

# Numerical assessment of the noise emission of Counter-Rotating Open Rotors

*L. Soulat<sup>\*†</sup> - I. Kernemp<sup>\*†</sup> - S. Moreau<sup>\*</sup> - R. Fernando<sup>†</sup>*

<sup>\*</sup>Université de Sherbrooke, Mechanical Engineering, Sherbrooke, QC, Canada

<sup>†</sup>Safran Snecma, Moissy-Cramayel, France

laurent.soulat@usherbrooke.ca, stephane.moreau@usherbrooke.ca

irwin.kernemp@snecma.fr, rasika.fernando@snecma.fr

## ABSTRACT

A hybrid method combining a three-dimensional unsteady RANS simulation of a cropped CROR at approach conditions and an acoustic analogy based on a frequency formulation of the Ffowcs-Williams and Hawkings' analogy, originally developed by Hanson and extended to non compact chord length, has shown three main sources, the impacts of the front-rotor wakes on the rear-rotor, of the front-rotor tip vortex on the rear-rotor tip, and of the front-rotor hub horse-shoe vortex on the rear-rotor foot. Consequently, this study confirms that the rear-rotor is the dominant tonal noise source and has identified another potential noise source when the CROR is installed caused by the strong tip vortex of the highly-loaded cropped rear-rotor. The rotor-rotor distance should not be reduced as the potential effect is already felt on the front rotor. The influence of the grid refinement has been evaluated on both aerodynamic and acoustic performances.

## NOMENCLATURE

$a$  ambient speed of sound

$B$  blade number

$c$  chord length

$D$  rotor diameter

$M_x$  axial Mach number

$M_r$  relative Mach number

$\Omega$  rotational speed

$\theta$  sideways angular position

$X_1$  front rotor quantity

$X_2$  aft rotor quantity

## INTRODUCTION

The use of Counter-Rotating Open Rotors (CROR) in low- to medium range transportation is seen as a good technique to improve significantly the specific fuel consumption of the next generations of aircrafts (M'Bengue, 2010). Nevertheless, acoustic design is very critical for this kind of configurations (e.g. Woodward, 1987) and has been a major obstacle so far. Indeed, the aerodynamic interactions between the two rotors are quite strong as shown by Podboy and Krupar (1989), generating an important noise over a very large spectrum and in all directions with a high tonality, contrarily to the classical turbfans where the duct around the fan will limit the noise propagation for some frequencies and directions. The rotor interactions can be decomposed into two distinct components. The first one is the tonal emission yielded by the periodic interactions of deterministic flow structures on each rotor. Tonal sources include the impingement of the wakes coming from the front rotor onto the downstream rotor blades, but also the wall pressure fluctuations induced on the front rotor by the

potential effects coming from the aft rotor. The second acoustic contribution is the broadband noise generated by the interaction of the random structures of turbulence with the blades and walls. As a matter of fact, the tonal noise is often the most disturbing feature because of the loud tones dominating a lower broadband noise. The precise understanding of the noise generation and propagation is therefore of prime importance to design the future CROR.

The main objective of the present study is to assess the numerical parameters to predict both aerodynamic performances and aeroacoustic tonal sources accurately.

## **CROR CONFIGURATION AND SIMULATION**

This study is based on the numerical analysis of the unsteady flow field for a generic  $12 \times 10$  CROR configuration (hub and blade geometries). Yet the latter does not take into account installation effects such as the pylone supporting the engine or the vicinity of the aircraft body or wings. Moreover, the ambient flow is supposed without general incidence relatively to the engine. The simulated configuration is represented in Fig. 1, along with the limit of the numerical domain used (hollow surfaces). The aft rotors is clipped (i.e. its diameter is reduced) in order to reduce the interaction with the wake of the front rotor in cruise conditions. The hub to tip ratio of the row is approximately 2. The front rotor diameter is approximately 4.2 m, the aft rotor being 10% smaller. The distance between the two rotors is approximately  $2c$ ,  $c$  being the front rotor chord length.

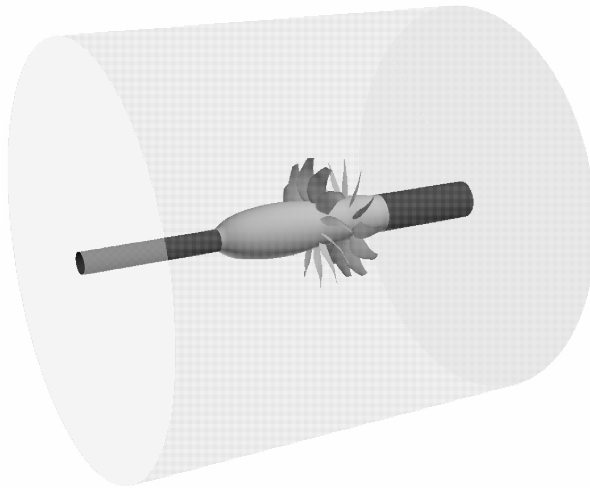


Figure 1: **CROR configuration**

The study has been performed in approach conditions. The advance Mach number is about  $M_x=0.2$ . Tip relative Mach number for the front rotor is approximately  $M_1=0.6$ . Both rotors turn at the same speed, with a quasi-equal torque split. Ambient pressure and temperature are set to  $P_s=101325$  Pa,  $T_s=303.15$  K respectively. These conditions were chosen because of the importance of noise emission during the take-off and landing phases. An additional goal of the present study is also to verify if the rotor clipping is enough in these new flow conditions.

### **Numerical simulation**

As stated previously, this study is based on the numerical simulation of the unsteady flow field around the CROR. Since the main objective here is to analyse the sources for tonal noise, it is not necessary to achieve a very high degree of accuracy in the prediction of the small vortical structures associated with turbulence. As a consequence, Unsteady Reynolds Average Navier-Stokes (URANS)

has been chosen to capture the deterministic features of the flow field at a reasonable numerical cost. The numerical domain is  $20c$  long upstream of the front rotor,  $15c$  long downstream of the aft one, and the outer diameter is approximately four times bigger than the front rotor diameter  $D$ . Using a mesh fine enough to reach a first cell dimensionless height  $y^+ = 5$ , there is about 5 million mesh points for the whole case (Fig. 2). Further grid refinement (especially in the rotor tip regions) did not yield significant improvement on the global integrated aerodynamic and acoustic parameters, as was recently found by Colin *et al* (Colin, 2012).

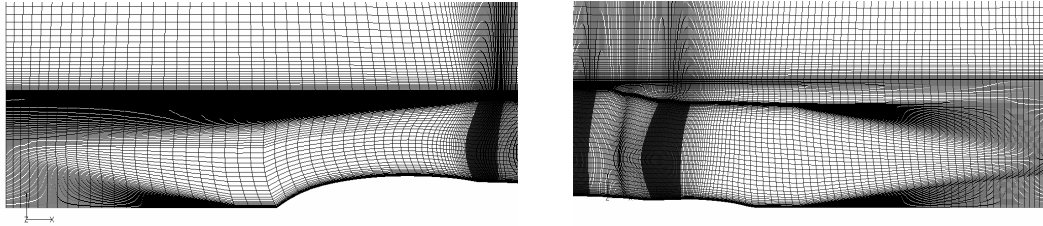


Figure 2: **Meridian view of the fine mesh**

Numerical simulations have been performed using the cell-centered structured solver Turb'Flow (Caro et al. 2003). Spatial discretization was performed using the second-order upwind AUSM+-up (Liou, 2006) scheme with the Van Albada limiter for the conservative variables (density, momentum and energy), whereas a first order upwind scheme was used for the turbulent flow-field. Kok's two equation  $k-\omega$  model (Kok, 2000) is used for turbulence coupled with Menter's turbulence kinetic energy production limiter (Menter, 1993). Time discretization is achieved using an explicit second-order 5-steps Runge-Kutta single time-stepping scheme.

The mesh does not physically move during the computation, the rotational effects (Coriolis and centrifugal forces) are directly taken into account as source terms in the URANS equations. The interface between the two rotors is achieved through a discrete Fourier decomposition and reconstruction of the flow field in the transverse direction; the relative movement of the rotors is simulated using a time variable offset in the flow-field reconstruction across the interface. This allows a complete unsteady communication between the interface blocks of each rotor. The other numerical boundaries bear either a no-slip wall conditions (blades and hub), a slip condition (far-field boundary), periodicity or an inlet/outlet conditions. Momentum and density are imposed at the inlet, whereas static equilibrium is set at the outlet. A 5% turbulence intensity is also imposed at the inlet.

Since the present solver does not perform chorochronic simulations, the number of blade on each rotor was set equal by adding two blades on the aft rotor to allow a periodic simulation of one blade on each rotor.

### **Acoustic model**

There are actually several possibilities to calculate the acoustic emission a CROR, ranging from simple and fast analytical models to complete but very costly direct numerical simulations. The chosen technique is the semi-analytical model proposed by Hanson (1985). This model predicts the far-field acoustic pressure  $p(x, r, \theta)$  for any CROR using the dipole source distribution over the blades. The thickness noise is neglected here, as well as the quadrupole contribution because of the

relatively low Mach number considered in this study. This models reads in the time domain :

$$\begin{aligned}
p(x, t) = & \frac{-i\rho a^2 B_2 \sin\theta}{8\pi(r_1/D)(1 - M_x \cos\theta)} \sum_{m=-\infty}^{\infty} \sum_{k=-\infty}^{\infty} \exp(i(mB_2 - kB_1)(\phi - \phi^{(2)} - \pi/2)) \\
& \times \exp(i(mB_2\Omega_2 + kB_1\Omega_1)(r/a - t)) \int_{hub}^{tip} M_r^2 \exp(i(\phi_0 + \phi_s)) \\
& \times J_{mB_2 - kB_1} \left[ \frac{(mB_2\Omega_2 + kB_1\Omega_1)z_0(D/(2a))\sin\theta}{1 - M_x \cos\theta} \right] \\
& \times \left[ k_x \frac{C_{Dk}}{2} \Psi_{Dk}(k_x) + k_y \frac{C_{Lk}}{2} \Psi_{Lk}(k_x) \right] dz_0
\end{aligned} \tag{1}$$

where

$$k_x = \frac{D/a}{M_r} \left[ \frac{mB_2\Omega_2 + kB_1\Omega_1}{1 - M_x \cos\theta} - kB_1(\Omega_2 + \Omega_1) \right] c/D \tag{2}$$

$$k_y = -\frac{2}{M_r} \left[ \frac{(mB_2\Omega_2 + kB_1\Omega_1)M_T \frac{D}{2a} z_0 \cos\theta}{1 - M_x \cos\theta} - \frac{(mB_2 - kB_1)M_x}{z_0} \right] c/D \tag{3}$$

$$\phi_s = \frac{D/a}{M_r} \left[ \frac{mB_2\Omega_2 + kB_1\Omega_1}{1 - M_x \cos\theta} - kB_1(\Omega_2 + \Omega_1) \right] \frac{MCA}{D} \tag{4}$$

$$\phi_0 = \frac{2}{M_r} \left[ \frac{(mB_2\Omega_2 + kB_1\Omega_1)M_T \frac{D}{2a} z_0 \cos\theta}{1 - M_x \cos\theta} - \frac{(mB_2 - kB_1)M_x}{z_0} \right] \frac{MCA}{D} \tag{5}$$

and MCA and FA are offset representing the sweep and lean of the blade respectively. Aside from the geometric definition of the configuration, the inputs of the model are the unsteady blade load distributions along the chord, expressed as an integral lift/drag coefficient  $C_{L/Dk}$  multiplied by a normalised distribution  $\Psi_{L/Dk}$ . In its original formulation, Hanson considered that the pressure variation along the chord was in phase, thus neglecting the time lag induced by the propagation of the flow structure along the blade. This was corrected here by expressing the distribution  $\Psi_{L/Dk}$  as complex values. In this study, the harmonic pressure distribution over the blades are extracted from the unsteady numerical simulation.

### Model comparison

The current implementation of Hanson's model has been compared to a second noise prediction technique, the analytical model recently proposed by Carazo et al. (2011). This model predicts the far-field noise of an open rotor subject to axial, transverse and radial loads. It relies on a compact description of the source, thus neglecting the distribution of the pressure fluctuations over the blade chord. Yet, it is able to take into account the three-dimensionnal shape of the blade, specifically the local sweep and lean angles of the blade. The acoustic response of the blade is constructed using a strip technique.

The comparison is achieved on an arbitrary simple blade geometry (different from the current CROR) with an arbitrary exponential source distribution along the chord  $p(x/c) = A \exp(-Ax/c)$ , where  $A=100$  here. The sources are emitting up to the fifth blade passing frequency harmonic with a constant amplitude. In Fig. 3 the noise levels and directivity of both models are sensibly the same, although the lobe pattern predicted using Carazo's model is smoother and flatter. The biggest differences occur for the first two harmonics. The agreement is even better for harmonics 4 and 5 (not shown). The differences are thought to be related to the different sources treatment, distributed along the chord for the present semi-analytical model, and compact for the other.

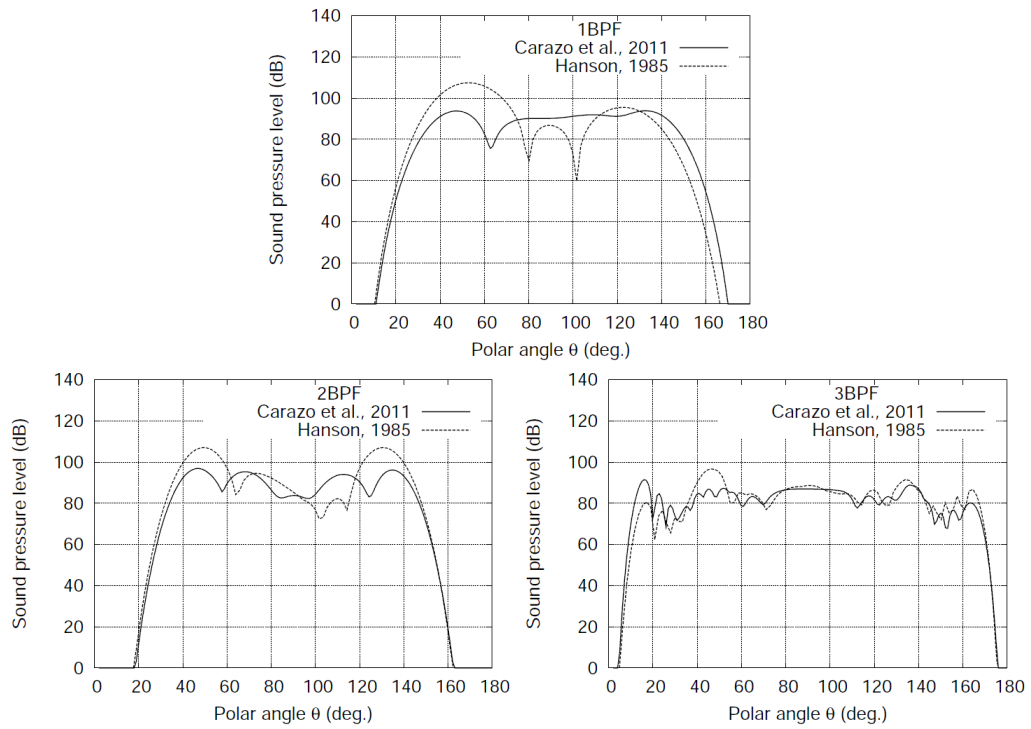


Figure 3: Comparison of the current extended Hanson's model to Carazo's model

### FLOW FIELD ANALYSIS

In the present case the global flow structure is rather simple. There is no particular shock wave or flow separation occurring on the two rotors, which is consistent with the approach conditions and a low incidence angle. Given the torque balance between the two rotors and the clipping of the second rotor, the aerodynamic load is higher on the aft blades. The second rotor operates properly, reducing the swirl generated by the front rotor as illustrated by the meridional view of the tangential velocity in Fig. 4-a. Yet, it is interesting to note that there is also an important positive swirl downstream the tip region of the aft rotor. As it will be seen later, this corresponds to the aft tip vortex. As expected, there is a contraction of the streamlines downstream of each rotor ("vena contracta" at approach).

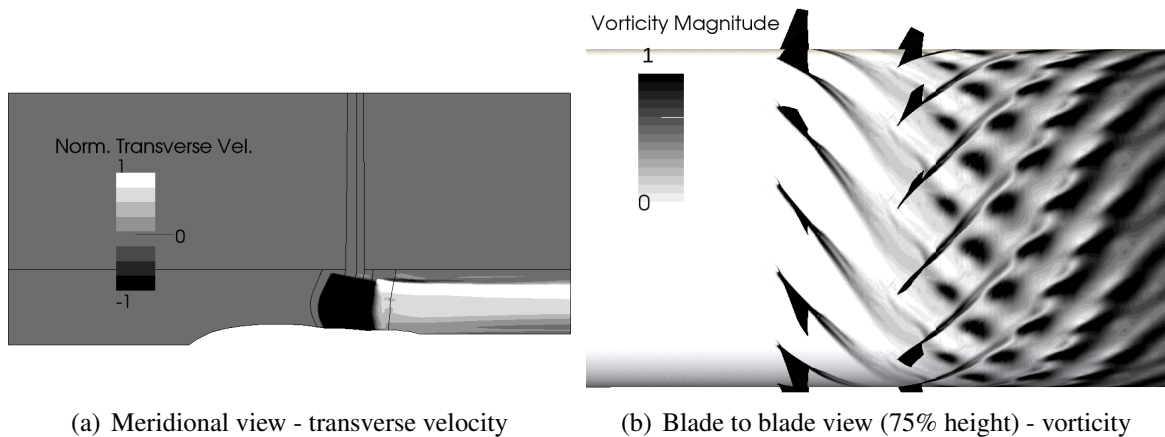


Figure 4: Flow fields for the CROR configuration

The unsteady flow structures are mainly characterised by the wake impingement of the front rotor on the aft rotor. A vorticity map in a blade to blade section clearly reveals the classical "chopping" of the front wakes by the aft blades (Fig. 4-b). When convected downstream, the front wakes progressively merge with the aft wakes yielding the checkerboard pattern observed downstream. It should already be stressed that the present simulations are fine and accurate enough to properly propagate these flow patterns far downstream.

### Vortical structures

As outlined in Fig. 4-a, the flow topology is also dominated by several strong vortical structures. The most important ones are the two tip vortices generated by the rotors. In Fig. 5-a, iso-surfaces of Q-criterion reveal that the tip vortex coming from the front rotor impinges on the second rotor at approximately 87% of the span, suggesting that more clipping on the aft rotor might be needed at approach. As for the classical viscous wake, this vortex is then chopped, but the resulting pieces keep a vortical structure as illustrated by the small patches of Q-criterion visible downstream of the aft rotor. The aft tip vortex is even bigger and stronger, which is consistent with the higher load on this rotor. The second tip vortex is slightly more "wavy" because of the interactions with the segments of the front rotor that are convected at a lower radius. This vortex is clearly visible up to 6c downstream of the aft rotor, which suggests that it could be an important noise generator for a puller configuration (i.e. an impact on the pylone located downstream).

The last noticeable structure is a small horseshoe vortex developing on the front rotor, outlined by an arrow in Fig. 5-a. This structure is mainly visible on the suction side of the blades. Although it decreases quite rapidly, the vortex is still visible up to the leading edge of the second rotor. Nevertheless, this structure completely disappears after impinging the aft blades.

### Mesh effects

The effects of mesh refinement were tested during the unsteady computation. A coarse mesh was generated by eliminating one point out of two in every direction from the current fine mesh. Another unsteady computation was then performed on this coarse mesh. A similar degree of convergence was achieved for both meshes.

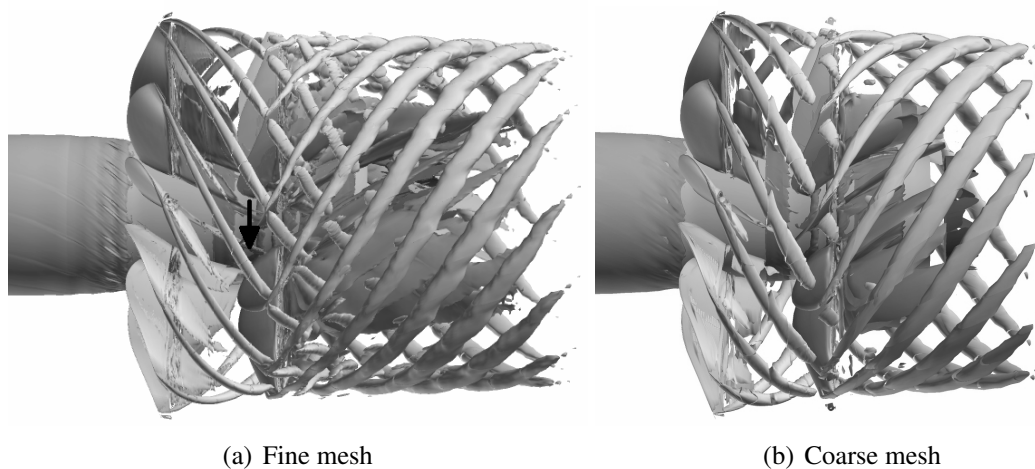


Figure 5: **Effect of mesh refinement on the flow structures**

The comparison of the flow fields reveals that there is a significant effect of the mesh on the different flow structures. The vortical structures are compared in Fig. 5. The coarse mesh in Fig. 5-b is

clearly responsible for an earlier dissipation of the structures, particularly the tip vortices. As a matter of fact, the tip vortex from the aft rotor disappears 30% faster (visible up to 4c downstream) on the coarse mesh. The front tip rotor is also weakened when impinging on the aft rotor, and the chopped segments disappear very quickly. As expected, the coarse mesh is also responsible for transverse growth of the vortices, with a 20% larger aft tip vortex. The viscous wake is altered in the same way by the mesh.

The mesh refinement does not modify the global characteristics of the flow significantly, such as the contraction behind the rotors and consequently the height of the vortex impingement on the aft rotor. The performances do not vary significantly. The thrust and efficiency, normalized by the value measured on the fine mesh are given in table 1. The finer mesh is a refined version of the fine mesh, with doubled point numbers on the blade skin blocks and in the inter row space, yielding an overall 8 million mesh points (5 millions for fine mesh).

Performance	Coarse mesh	Fine mesh	Finer mesh
Norm. Thrust	99.0%	100%	100.3%
Norm. Efficiency	99.1%	100%	100.5%
Norm. Torque Split	99.8%	100%	100.1%

Table 1: **Effect of mesh refinement on CROR performances**

## ACOUSTIC ANALYSIS

### Source analysis

The precise determination of the acoustic sources is of prime importance for a correct noise prediction. Interestingly, the harmonic load distributions e.g. the sources, have to be determined for noise prediction using Eq. (1), and are therefore directly available for study. The first five loading harmonic, thereafter noted 0BPF, 1BPF, 2BPF, 3BPF, 4BPF and 5BPF are presented in Fig. 6 for each blade in normalised amplitude. The normalisation is achieved by dividing all the pressure levels by the maximum read for the fifth harmonic. The frequencies used for the harmonic decomposition are the blade passing frequency (BPF) and following sub-harmonics  $(kB_1\Omega_1 + mB_2\Omega_2), \forall k, m$ . Load harmonic 0BPF is the steady loading of the blade. Although constant, 0BPF is responsible for the rotor loading noise at frequencies  $kB_{1/2}\Omega_{1/2}, \forall k$  because of the unsteadiness introduced by the blade movement.

As expected, the steady loading 0BPF is mainly concentrated near the leading edge of each blade, and the aft rotor loading is higher than the front one. Moreover, the amplitude of the steady loading is a hundred times larger than the following loading harmonics.

Considering the first truly unsteady load harmonic (1BPF), the pressure fluctuation over the aft rotor are ten times stronger than on the front rotor. This confirms that the wake and vortex impingement on the aft blade are far more energetic than the interaction of the potential effects with the front rotor. The fluctuations on the aft rotor are located mainly near the leading edge, except in the root and tip regions. This suggests that the wake intensity decreases quickly after the impingement. The effects of the front tip vortex are particularly clear here, maximising the pressure fluctuation above 80% of the span. The tip vortex interaction is also responsible for a spread of the pressure fluctuations over the whole chord in the tip region. The impact of the small horse-shoe vortex is also visible, with another strong fluctuation-increase near the blade root. Although weaker, the potential effects on the front blade are not negligible either. The unsteady load-topology is somehow different for this rotor, with a better spread of the fluctuations all over the blade surface. The maximum fluctuation is located in the upper half of the blade, at mid-chord.

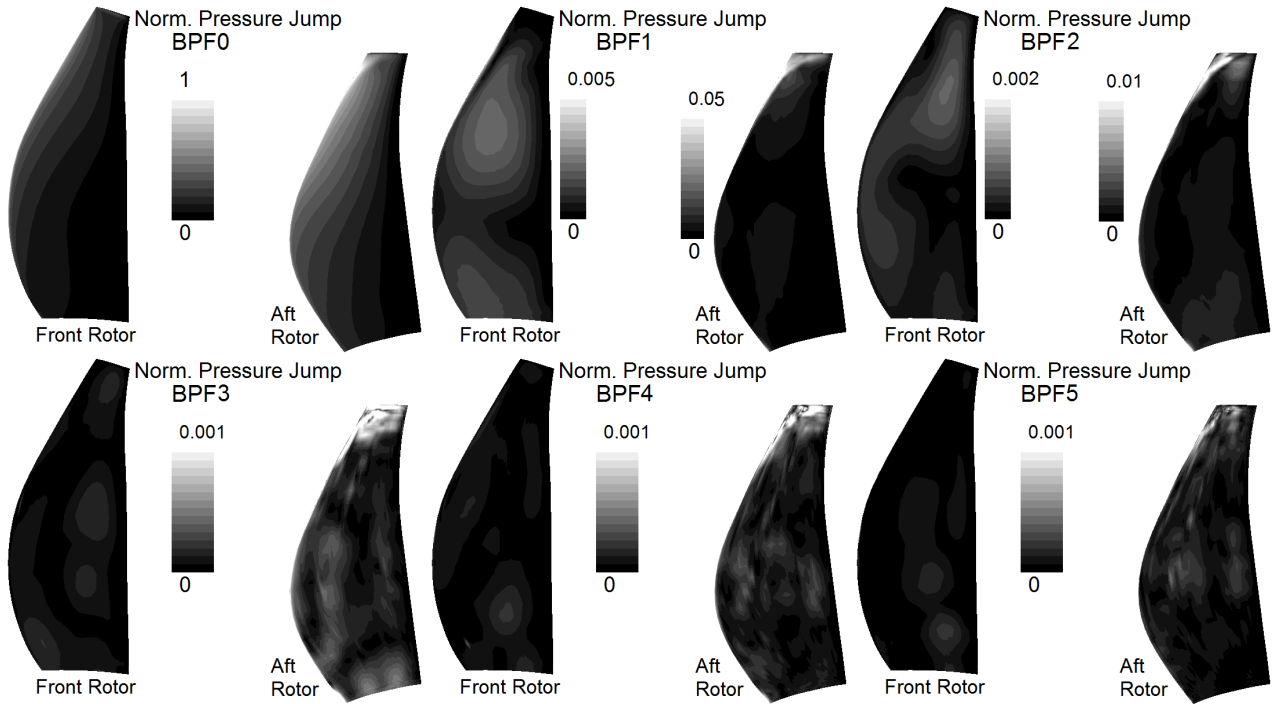


Figure 6: Dipolar source distribution over the blades. Harmonics ranked from 0 to 5

The fluctuations associated with the second loading harmonic 2BPF are decreasing progressively compared to 0BPF and 1BPF. Again, the levels seen on the aft rotor remain much higher than on the front rotor, and the potential effects are still visible on the front blade. The topology on the front rotor is slightly different from the one observed for 1BPF, with the maximum fluctuations located above 60% span, near the blade trailing edge. The global topology on the aft rotor is the same, but some small differences appear. The impact of the tip vortex now generates a maximum fluctuation near the leading edge only, quickly decreasing along the chord.

The rotor-rotor interactions can be traced up to the third order for the aft rotor and to the second order for the front one. As illustrated in Fig. 6, the loading fluctuations for 4BPF and 5BPF seem a little "noisier", with a low amplitude. Using 75 time steps per blade passing period, the sampling frequency for the 4BPF (resp. 5BPF) fluctuation is only 18.75 (resp. 15) samples per period, which is relatively low. Consequently, the numerical errors cannot be neglected any more. Nevertheless, it should be noted that the impacts of the vortices on the aft blades are still clearly visible up to 5BPF, confirming that these interaction-mechanisms are probably the most effective from an acoustical point of view.

#### Mesh refinement effects

The effects of the mesh refinement on the pressure fluctuations were also studied. The comparison of the pressure distribution in Fig. 7 shows that the mesh refinement has almost no effect on the prediction of the steady loading confirming the negligible impact on the wake contraction and the overall performances, but it yields large discrepancies on the unsteady fluctuations, with 1BPF amplitudes up to 50% lower on the coarse mesh, particularly in the tip region. This sensitivity justifies the grid refinement study performed in this region to yield the final fine mesh. These discrepancies are even higher for the following loading harmonics. This ultimately yields a global 7dB underprediction for the noise computation on the coarse grid, with differences in the directivity ranging from 5dB to

15dB. This proves that the coarse mesh could be a good compromise for performance prediction of the machine (thrust, efficiency,etc. . . ), but is definitely not acceptable for the noise predictions.

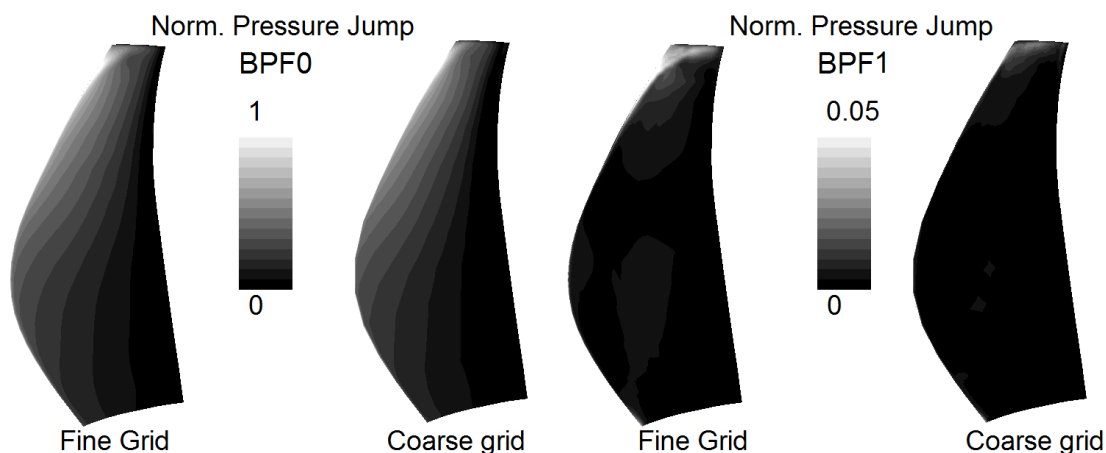


Figure 7: Mesh refinement effects on the pressure distributions for 0 and 1BPF - aft rotor

### Noise prediction

Using the modified Hanson model (Eq. (1)), it is now possible to predict the far field noise for this configuration. The acoustic directivities are evaluated along a sideline  $10 \cdot D$  away from the CROR. The overall acoustic sound pressure level (OASPL) directivity and the directivity of a few modes are given in Fig. 8. The polar angle  $\theta = 0^\circ$  represents the front of the CROR. As expected from the source analysis, the noise emitted by the aft rotor is louder than the front rotor by 20dB in average. Both rotors emit on the CROR axis, which is consistent with the present assumption of an equal number of blades on each row. Considering the detailed directivity of each rotor, the steady loading

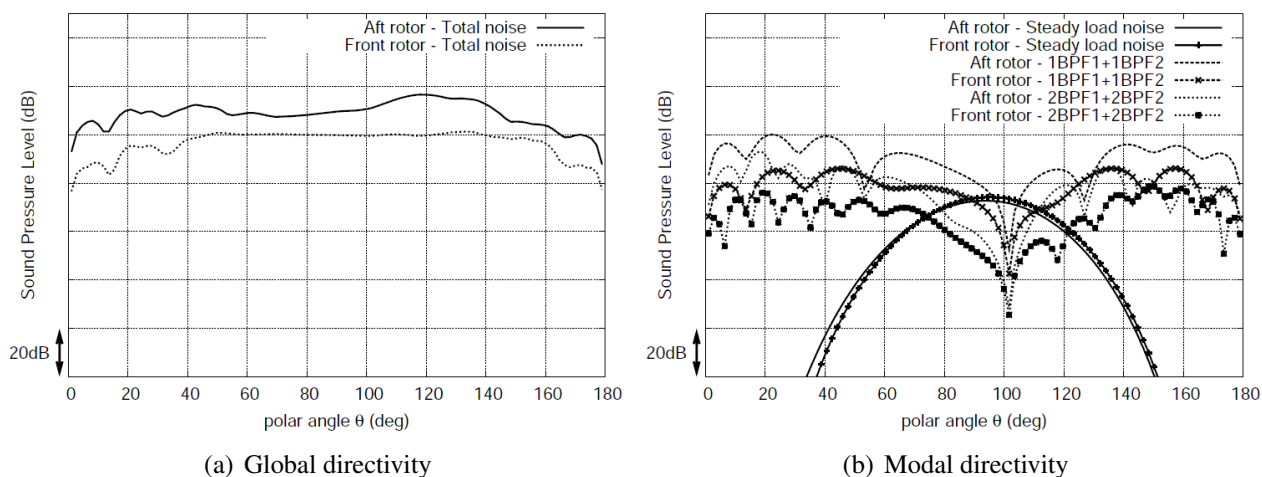
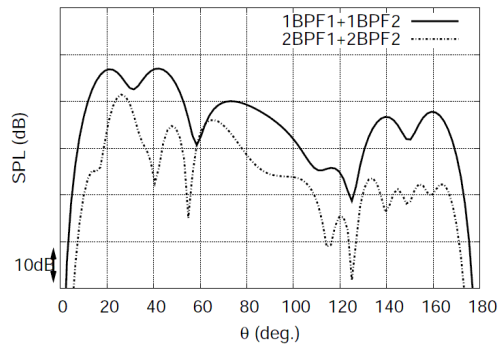


Figure 8: Noise prediction for the CROR configuration

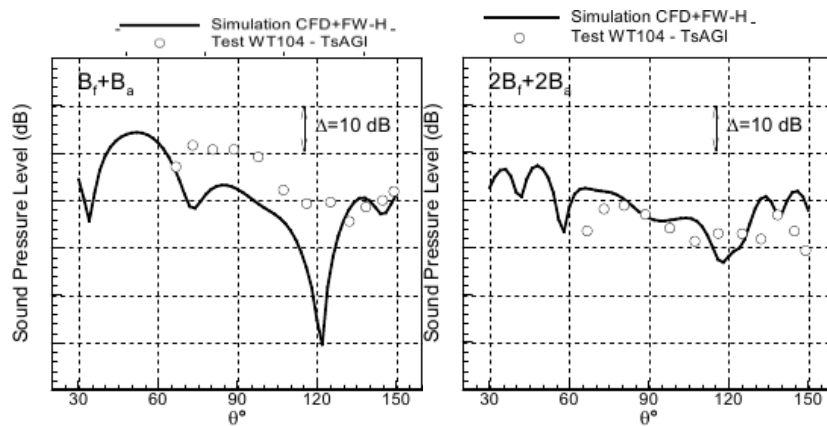
noise is visible as the symmetric lobe located around  $\theta = 90^\circ$ . Once again, the aft rotor noise is higher, but only marginally compared with the front rotor (a few decibels only). The main difference is for the interaction modes  $1BPF_1+1BPF_2$  and  $2BPF_1+2BPF_2$ . The 20dB difference between the two rotors is clearly visible, confirming that the wake and vortex interaction is the most important

mechanism for noise generation. The interaction noise are even higher than the steady blade loading. The directivity patterns have several lobes for each rotor. Noise emission is globally stronger upstream of the CROR, which is thought to be related to the source concentration near the leading edges of the blades. The modal analysis also confirms that the interaction modes are responsible for the acoustic emission along the rotational axis of the CROR. As predicted before, the mesh refinement do have a noticeable effect on the noise emission. Although the directivity patterns do not change, the sound level is under-estimated by almost 10dB using the coarse mesh. This finally proves the importance of a precise spatial discretization for the acoustical analysis.

Using the modified Hanson’s model, it is simple to evaluate the effects of a variation of the blade numbers, as long as this variation does not affect the flow on the rotor significantly (e.g. a low solidity variation). The noise emission has been calculated when  $B_2$  is reduced to 10. The resulting configuration is actually close to another CROR tested at DLR in similar flight conditions. The current noise prediction is compared with those presented by Schnell et. al (2012) in Fig. 9. Compared to the experimental and numerical results obtained at DLR/TsaGi, the current study predicts the directivity of the CROR fairly well. The only differences are an increased number of lobes for  $\theta \geq 100^\circ$  and slightly more amplitudes of the dips. This might be caused by a slightly different blade loading.



(a) Current study



(b) From Schnell et al (2012)

Figure 9: Comparison with the results of Schnell et. al (2012)

## CONCLUSIONS

A hybrid method combining a three-dimensional unsteady RANS simulation and an acoustic analogy based on a frequency formulation of the Ffowcs-Williams and Hawkings’ analogy, originally developed by Hanson and extended to non compact chord length, has been successfully applied to

a realistic cropped CROR at approach conditions. The unsteady simulation has been achieved for a  $B_1=B_2$  configuration on one sector but the noise predictions have been achieved for both  $B_2$  and  $B_2-2$  rear rotor blades. The unsteady flow field shows several strong vortical structures, namely the wakes of both rotors, the horse-shoe vortex at the blade root of the front rotor and the strong tip vortices of both rotors. The unsteady blade loading on the cropped rear-rotor consequently show three zones of strong interaction: the tip region is strongly affected by the impact of the front-rotor tip vortex caused by the vena contracta at approach condition; the hub region also shows the strong impact of the horse-shoe vortex formed on the front-rotor; finally the rest of the blade exhibits strong fluctuations caused by the impact of the front-rotor wake. All these pressure fluctuations are however concentrated at the leading edges of the rear-blades. The flow analysis also shows some significant potential effect of the rear-rotor on the front front. Finally the strength of the tip vortex of the rear-rotor caused by the high loading of the cropped blade yield a strong vorticity layer that could cause a secondary noise source by impingement on some downstream empennage or some strong contrail vortices. The implementation of the acoustic model has been successfully compared with a model recently developed by Carazo *et al.* Consistent results have also been obtained with acoustic measurements on similar configurations. The mesh is seen to have a major impact on the acoustic levels and directivity shape predicted by the method, and a mesh of at least 5 million points should be used that properly resolved the boundary layers on both rotors and the rotor wake interaction. The acoustic signature also confirms the different noise sources identified in the unsteady flow analysis and shows a dominant contribution of the rear-rotor acoustic radiation.

## ACKNOWLEDGEMENTS

We wish to acknowledge the financial support of SNECMA Groupe Safran, the technical support from Fluorem on Turb'Flow, and Compute Canada and the RQCHP (Réseau Québécois de Calcul de Haute Performance) for providing the necessary computational resources.

## REFERENCES

- [1] A. Carazo, M. Roger, and M. Omais. Analytical prediction of wake-interaction noise in counter-rotation open rotors. In *17th AIAA/CEAS Aeroacoustics Conference(32nd AIAA Aeroacoustics Conference)*, [2011]. AIAA 2011-2758.
- [2] J. Caro, P. Ferrand, S. Aubert, and L. Kozuch. Inlet conditions effects on tip clearance vortex in transonic compressor. In *Proceedings of 5th European Conference on Turbomachinery Fluid Dynamics and Thermodynamics*, Prague, [2003].
- [3] Y. Colin, F. Blanc, B. Caruelle, F. Barrois, and N. Djordjevic. Computational strategy for predicting cror noise at low-speed part ii: investigation of the noise sources computation with the chorochronic method.
- [4] D.B. Hanson. Noise of counter-rotation propellers. *Journal of Aircraft*, 22(7):609–617, [1985].
- [5] J.C. Kok. Resolving the dependence on free-stream values for the  $k-\omega$  turbulence model. *AIAA Journal*, 38(7).
- [6] M.S. Liou. A sequel to ausm, part ii: Ausm+up for all speed. *Journal of Computational Physics*, 214:137–170, [2006].
- [7] L. M'Bengue. Towards acare 2020 : Innovative engine architectures to achieve the environmental goals.

- [8] F.R. Menter. Zonal two equation  $k$ - $\epsilon$  turbulence models for aerodynamic flows.
- [9] G.G. Podboy and M.J. Krupar. Laser velocimeter measurements of the flowfield generated by an advanced counterrotating propeller. Technical Report NASA-TM-01437, [1989].
- [10] R. Schnell, J. Yin, S. Funke, and H. Siller. Aerodynamic and basic acoustic optimization of a contra- rotating open rotor with experimental verification.
- [11] R.P. Woodward. Noise of a model high speed counterrotation propeller at simulated take-off/approach conditions ( $f7/a7$ ). Technical Report NASA-TM-100206, [1987].